ADVANCED ENGINEERING MATERIALS
www.aem-journal.com

Effect of Zn Addition on Phase Evolution in AlCrFeCoNiZn High-Entropy Alloy

Vikas Shivam, Dishant Beniwal, Yagnesh Shadangi, Prashant Singh, Olena Palasyuk, V. S. Hariharan, Matthew J. Kramer, Gandham Phanikumar, Duane D. Johnson, Pratik K. Ray,* and Nilay Krishna Mukhopadhyay*

The addition of Zn to AlCrFeCoNi high-entropy alloy (HEA) poses intriguing questions as to how it would affect phase evolution. Herein, the phase evolution in AlCrFeCoNiZn is studied using a combination of experimental techniques (X-ray diffraction, scanning electron microscopy, energy-dispersive spectroscopy, and differential scanning calorimetry) and computational (density-functional theory [DFT], calculation of phase diagrams, and machine-learning) methods. Mechanically alloyed and spark-plasma-sintered AlCrFeCoNiZn assumes a metastable single-phase, body-centered-cubic (BCC) structure that undergoes diffusion-controlled phase separation upon subsequent heat treatment to form separate (Al, Cr)-rich, (Fe, Co)-rich, and (Zn, Ni)-rich phases. The formation of (Al, Cr)-rich phase, not reported previously in AlCrFeCoNi-based HEAs, is attributed to strong clustering tendency of Cr–Zn and Cr–Ni pairs, combined with the strong ordering of Zn–Ni pair, driving out Cr that in turn combines with Al to form a (Al, Cr)-rich phase. In the DFT results, the formation of thermodynamically stable $L1_2$ phase is shown wherein Cr–Fe–Zn [Al–Ni-Co] preferably occupy1a (000) [3c (0 ½ ½)] positions. The sluggish diffusional transformation to $L1_2$ phase from BCC precursors is attributed to the small stacking-fault energy of AlCrFeCoNiZn. The equilibrated HEA exhibits a high microhardness of 8.24 GPa with an elastic modulus of 184 GPa.

1. Introduction

High-entropy alloys (HEAs), from their inception,[1,2] have garnered significant attention due to their superior thermodynamic, structural, and mechanical properties over conventional alloys.[3–6] Recently, Li et al.[7] have shown that mixing entropy alone is not sufficient to improve structure–property correlations in HEAs. The study introduces the idea of metastability created by compositional imbalance that significantly improved the mechanical properties of HEAs, opening exciting avenues for tailoring microstructure.[7–10] This suggests that competing effects of entropy, formation enthalpy, short-range ordering (SRO), and lattice strain (atomic-size mismatch) should be given due consideration for assessing thermodynamic stability and mechanical properties.[9,11–13] While the well-quantified rules governing phase evolution in HEAs are still an open question, the face-centered-cubic ↔ body-centered-cubic (FCC ↔ BCC) transitions in HEAs have been linked strongly to valence-electron count

V. Shivam, D. Beniwal, P. K. Ray
Department of Metallurgical and Materials Engineering
Indian Institute of Technology Ropar
Rupnagar 140001, Punjab, India
E-mail: vikas.rs.met13@iitbhu.ac.in; pratik@iitrpr.ac.in

V. Shivam
Department of Materials Science and Engineering
Seoul National University
Seoul 08826, Republic of Korea

Y. Shadangi, N. K. Mukhopadhyay
Department of Metallurgical Engineering
Indian Institute of Technology (BHU)
Varanasi 221005, Uttar Pradesh, India

Y. Shadangi
Department of Materials Science and Metallurgical Engineering
Indian Institute of Technology Bhilai
Durg 491001, Chhatishgarh, India

The ORCID identification number(s) for the author(s) of this article can be found under https://doi.org/10.1002/adem.202400827.

DOI: 10.1002/adem.202400827

P. Singh, O. Palasyuk, M. J. Kramer, D. D. Johnson
US Department of Energy
Ames Laboratory
Ames, IA 50011, USA

V. S. Hariharan, G. Phanikumar
Department of Metallurgical and Materials Engineering
Indian Institute of Technology Madras
Chennai 600036, Tamil Nadu, India

D. D. Johnson
Department of Materials Science & Engineering
Iowa State University
Ames, IA 50011, USA

(VEC)[14–16] wherein VEC < 6.87, $6.87 \leq$ VEC < 8, and VEC ≥ 8 are generally associated with the formation of BCC, mixed FCC + BCC, and FCC phases, respectively.[15] CrFeCoNi-based alloy systems have been among the most widely studied HEAs.[17–20] Addition of Al, with low VEC of 3, drives the transition from a single-phase FCC structure in CrFeCoNi (VEC = 8) to a BCC structure in AlCrFeCoNi (VEC = 7.2).[21,22] In contrast, Zn, with its high VEC of 12, shows drastically different bonding tendencies with elements present in CrFeCoNi wherein it bonds strongly with Co and Ni and clusters strongly with Cr and Fe. Moreover, Zn is not a typical 3*d*-transition metal owing to its completely filled *d*-orbitals. This contrasting behavior of Zn and Al makes it interesting to observe phase evolution when both Al and Zn are added together to CrFeCoNi. With this as motivation, we present an in-depth study into the phase evolution in equiatomic AlCrFeCoNiZn.

The low boiling point of Zn, which is lower than the melting point of other elements here (except Al), makes the casting of AlCrFeCoNiZn challenging. Thus, mechanically alloyed + spark plasma sintered (MA + SPS) route has been used for alloy fabrication. MA is a well-known technique to develop nanocrystalline alloys, oxide-dispersion-strengthened alloys, quasicrystals, amorphous alloys, and composites with homogenous microstructure and extended solid solubility.[23–25] HEAs synthesized by MA have better mechanical properties due to grain refinement and solid-solution strengthening with homogenous mixing of alloying elements.[26–30] SPS is a solid-state sintering technique used for consolidation of alloyed powder prepared through MA. It is based on the concept of Joule heating wherein a high amperage current is passed to produce thermal energy that rapidly increases the material's temperature to form a dense product of nanometric grains.

The choice of processing route (as-cast or MA + SPS) can lead to different microstructures for the same HEA. As-cast AlCrFeCoNi HEA has a BCC structure with small amounts of (Al, Ni)-rich ordered B2 phase, and heat treatment at 850 °C for 3 h results in formation of new FCC and sigma (σ) phases along with the BCC and B2 phases.[31,32] The σ phase is stable over a relatively small temperature range (roughly from 600 to 975 °C) while the FCC remains stable up to 1200 °C. AlCrFeCoNi prepared through MA + SPS (at 1000 °C with a dwell time of 6°/min) shows formation of an FCC solid-solution phase along with the precipitation of nano-sized (Fe, Co, Cr)-rich σ phase and (Al, Ni)-rich $L1_2$ phase.[33] Atom probe and transmission electron microscopy (TEM) studies at nanometer scale have also confirmed phase separation in AlCrFeCoNi, driven by elemental segregation owing to strong Al–Ni and Fe–Cr ordering tendencies.[34]

In view of this, the idea of Zn addition to AlCrFeCoNi poses some interesting and open questions with respect to the phase evolution in AlCrFeCoNiZn alloy: 1) Zn addition considerably increases the VEC from a value of 7.2 for AlCrFeCoNi to 8 for AlCrFeCoNiZn. From the VEC-based phase-selection criterion,[15] wherein VEC ≥ 8 is generally associated with the formation of simple FCC solid-solution phases, will Zn addition destabilize BCC AlCrFeCoNi to form FCC or mixed phases? 2) Miedema's chemical enthalpies for binary pairs (i.e., subregular interaction parameters) indicate that both Zn and Al tend to bond strongly with Ni whereas Zn tends to cluster weakly with Al. One can therefore question the coexistence of (Al, Ni, Zn) in a single phase, and whether Zn added to AlCrFeCoNi HEA will form (Al, Ni, Zn)-rich phase or a segregated (Zn, Ni)-rich and (Al, Ni)-rich phases; and 3) The Zn addition is expected to change the phase evolution in AlCrFeCoNi due to change in local thermodynamic SRO, i.e., ordering or clustering type. How these thermodynamic changes might impact the formation of σ (Fe–Co–Cr rich) is not well understood. Furthermore, owing to large ordering tendency of Al–Ni pair, we usually do not expect the formation of new (Al, Cr)-rich ordering phases in AlCoCrFeNi-based HEAs. But Zn addition might affect this behavior; however, to the best of our knowledge, there are no such theoretical or experimental reports yet.

With these questions as the backdrop, we have performed an in-depth analysis of the phase evolution in AlCrFeCoNiZn. The multi-principal nature of HEAs necessitates the understanding of the phase evolution in different time–temperature scales. The type of phases and their fractions solely decided the properties of the materials. Moreover, the adoption of phase evolution in HEAs into engineering applications, especially alternatives to superalloys, will likely necessitate looking beyond single-phase solid-solution strengthening to achieve competitive results.[35] Pretrained machine-learning (ML) models and calculation of phase diagrams (CALPHAD) approaches have been used to establish preliminary expectations of phase transitions, whereas X-ray diffraction (XRD) and energy-dispersive spectroscopy (EDS) data have been analyzed for the identification of phase structures and elemental segregation. Density-functional theory (DFT) calculations have been used to probe the drivers for phase transitions and elemental segregation. Because SPS may not lead to formation of equilibrium structures, the effect of different heat treatments has also been studied. The insights gained from our work not only advance the understanding of this particular alloy, but also expand the general phase-selection principles for HEAs where strong ordering and clustering pairs are present.

2. Results and Discussion

2.1. ML and CALPHAD Predictions

A pretrained ML model,[36] built for as-cast alloys, was used for a preliminary probe into the phase evolution starting with equiatomic CrFeCoNi as the base composition and we calculated the effect of separate or simultaneous addition of Al and Zn. **Figure 1**a–d shows FCC, BCC, and IM phase fractions predicted. $Al_x(CoCrFeNi)_{1-x}$ has been extensively studied[17,18] and the model predictions (Figure 1a) match the reported transition from FCC to BCC structure with Al addition. The model predicts significant IM formation with addition of Zn to CrFeCoNi (Figure 1b), which could be due to the elemental segregation promoted by Zn as it has a strong tendency to cluster with Cr and Fe; this is supported by large positive values of Miedema's chemical enthalpy of mixing for Zn–Cr and Zn–Fe binary pairs in Figure 1e. Addition of Al to CrFeCoNiZn is predicted to further increase the IM formation (Figure 1c), indicating that Al further promotes the elemental segregation caused by Zn. One can also observe that increasing Al content results in an increase in BCC phase fraction, which is similar (albeit to a lower extent) as experimental observations in the AlCrFeCoNi

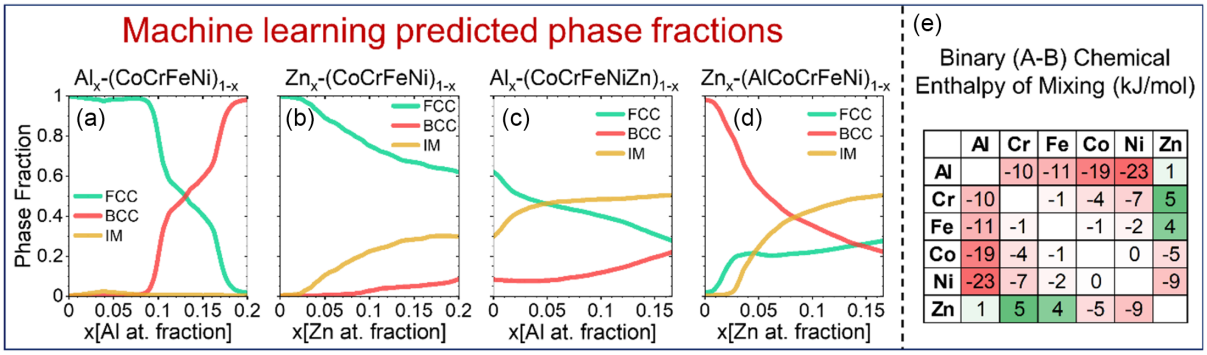

	Al	Cr	Fe	Co	Ni	Zn
Al		-10	-11	-19	-23	1
Cr	-10		-1	-4	-7	5
Fe	-11	-1		-1	-2	4
Co	-19	-4	-1		0	-5
Ni	-23	-7	-2	0		-9
Zn	1	5	4	-5	-9	

Figure 1. FCC, BCC, and intermetallic (IM) phase fractions predicted by pretrained ML model in a) Al$_x$–(CoCrFeNi)$_{1-x}$, b) Zn$_x$–(CoCrFeNi)$_{1-x}$, c) Al$_x$–(CoCrFeNiZn)$_{1-x}$, and d) Zn$_x$–(AlCoCrFeNi)$_{1-x}$ alloy systems. e) Miedema's chemical enthalpy of mixing for binary pairs in solid-solution phase.

system. Addition of Zn to AlCrFeCoNi (which has single-phase BCC structure) is predicted to initiate the formation of a new FCC phase at low Zn content up to 3 at% (Figure 1d). With further Zn addition, the FCC phase fraction is predicted to remain fairly constant (approximately 20%) while the BCC phase is predicted to dissociate resulting in formation of a significant amount of IM phases, along with BCC and FCC phases, in equiatomic AlCrFeCoNiZn. This is intriguing as this provides us insights that Zn-doped AlCrFeCoNi alloys may actually have significantly higher hardness due to the presence of a large amount of IM(s) as well as a BCC phase that should have a smaller number of slip systems as compared to the FCC phase—which we have tested experimentally and presented later in this section. In short, the ML model provides two key predictions—first, that Zn in CrFeCoNi will cause significant IM formation and, second, that combining Al with Zn will further promote the IM formation.

While the ML model[36] is capable of probing phase fractions along compositional variations, it cannot predict: 1) the effect of temperature as it was built for as-cast alloys at room temperature; and 2) the elemental composition of individual phases. Because the alloy samples are prepared using SPS and also heat-treated later, we used CALPHAD to predict the effect of temperature on the composition and transition of phases. **Figure 2** shows the CALPHAD predictions for AlCrFeCoNiZn. The key predictions from these results are: 1) the entire Zn content in the alloy segregates with Ni to form a $Zn_{3.55}Ni$ IM (GAMMA_D83, structure type—Cu_9Al_4, Figure 2f), which is stable from room temperature to its melting point of 780 °C; 2) formation of separate Cr-rich (BCC_B2#1, Figure 2b) and Fe-rich

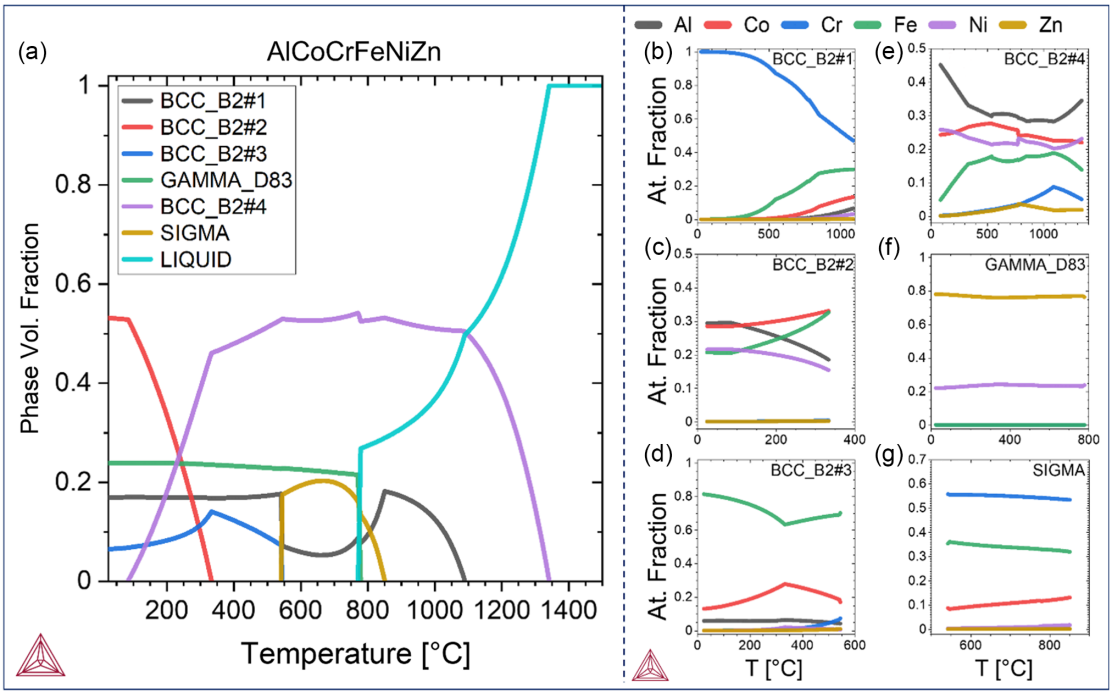

Figure 2. CALPHAD predictions for phase transitions and phase compositions versus temperature in AlCrFeCoNiZn. a) Volume fraction of phases as a function of temperature. b–g) Elemental composition of each phase as a function of temperature over the temperature range where it is stable.

(BCC_B2#3, Figure 2d) phases that remain stable from room temperature to 542 °C, where they combine to form a (Cr, Fe)-rich σ phase (SIGMA, Figure 2g) that remains stable up to 852 °C; and 3) entire Al content in the alloy segregates into (BCC/B2)-type phases (BCC_B2#2 & BCC_B2#4, Figure 2c,e), which are almost Cr and Zn free. We note that in AlCrFeCoNi (Figure S1, Supporting Information), where Zn is not present, CALPHAD does not predict formation of (Fe, Co)-rich BCC/B2 phase. The exceptional tendency of Zn to preferentially segregate with Ni might be a driver for this behavior as formation of (Zn, Ni)-rich IM would deplete Ni in the BCC/B2 phase; and as Ni is a high VEC element, Fe and Co (with lower VEC than Ni) might segregate to maintain the stability of primary BCC/B2 phase that has Al. In effect, the comparison between CALPHAD predictions for AlCrFeCoNi and AlCrFeCoNiZn suggests that Zn might segregate almost exclusively with Ni and a (Fe, Co)-rich might form in AlCrFeCoNiZn. While these calculations give needed insights, it is important to be mindful of two discrepancies in these CALPHAD predictions: 1) almost pure Cr is predicted as a separate phase (BCC_B2#1, Figure 2b) but such behavior has not been reported in any experimental or *ab initio* studies; and 2) partial melting of AlCrFeCoNiZn is predicted to start at 780 °C, but no melting was observed in the sample during heat treatment at 900 °C or in DSC thermogram in this temperature range (i.e., under 1100 °C). This also highlights a key challenge in the modelling of HEAs that arises due to the astronomically large compositional space that has to be probed with relatively scarce data as compared to traditional alloys. One way to address this is by borrowing the best from different models. While ML models excel at determining the as-cast phase selection and properties at room temperature,[36–39] CALPHAD is often more reliable at high temperatures. While DFT calculations are unmatched in their accuracy and reliability, ML and CALPHAD offer vastly better high-throughput capabilities. Thus, rather than relying on a single technique, we have implemented multiple modeling tools here to identify relative consistencies across the techniques.

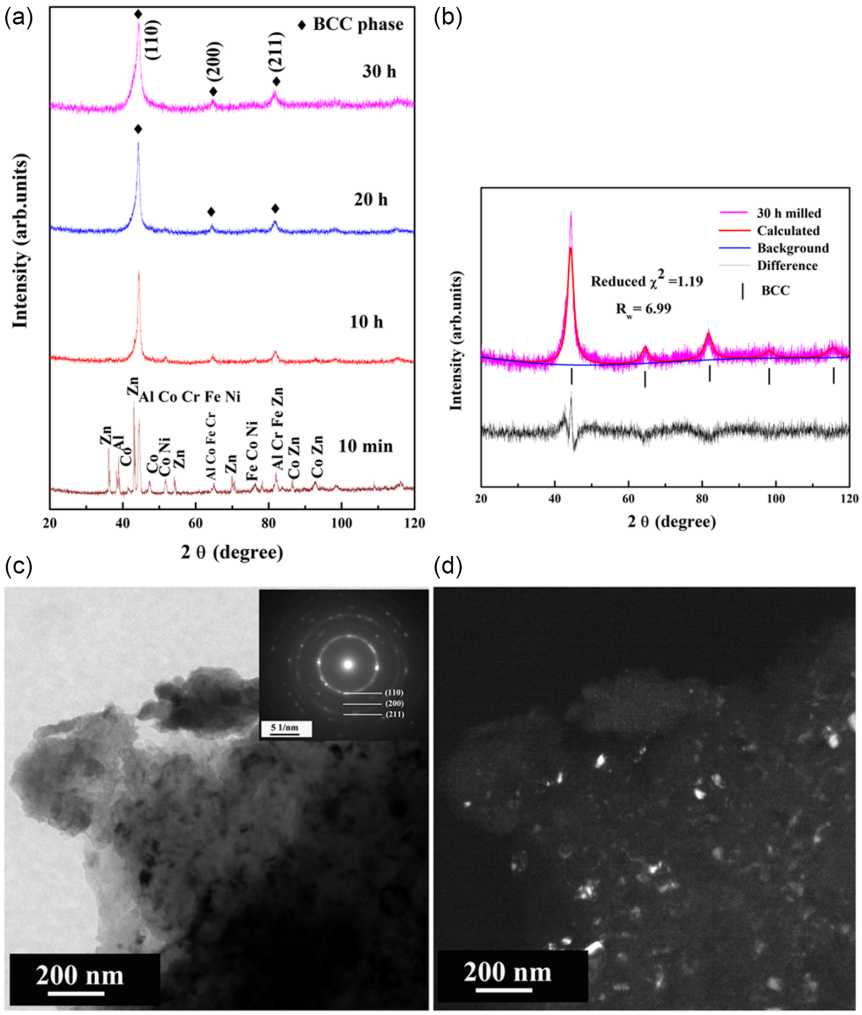

Figure 3. Structure evolution during milling process. a) X-ray diffraction patterns of AlCrFeCoNiZn HEA powder milled up to 30 h. The evolution of the single-phase BCC structure is discerned, b) full pattern refinement of 30 h milled powder sample, c) TEM bright-field image (inset gives the SADP), and d) dark-field image of 30 h milled sample.

2.2. Characterization Using XRD

The diffraction patterns of milled AlCrFeCoNiZn powder at different milling durations are shown in **Figure 3**a. At the start of milling process (after 10 min), peaks corresponding to all constituent elements were observed. As milling proceeds for 10 h, the peaks broadened and the intensity of most peaks decreased significantly, confirming alloying of the elements

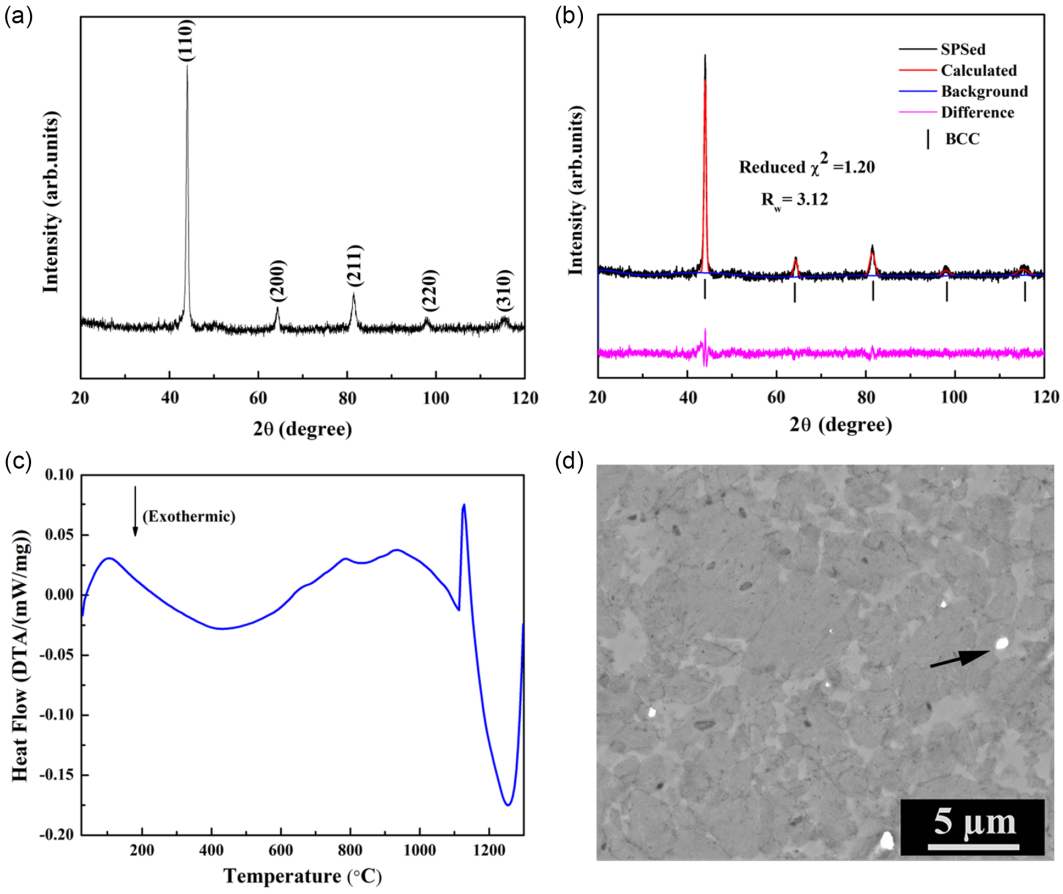

Figure 4. Structure and thermal stability of SPS-prepared AlCrFeCoNi alloy. a) X-ray diffraction pattern of SPSed AlCrFeCoNiZn HEA sintered at 800 °C, b) full pattern refinement of SPSed sample, c) the DSC thermogram of the SPSed sample heated up to 1300 °C, and d) SEM micrograph of the SPSed sample (arrow shows the alumina particle).

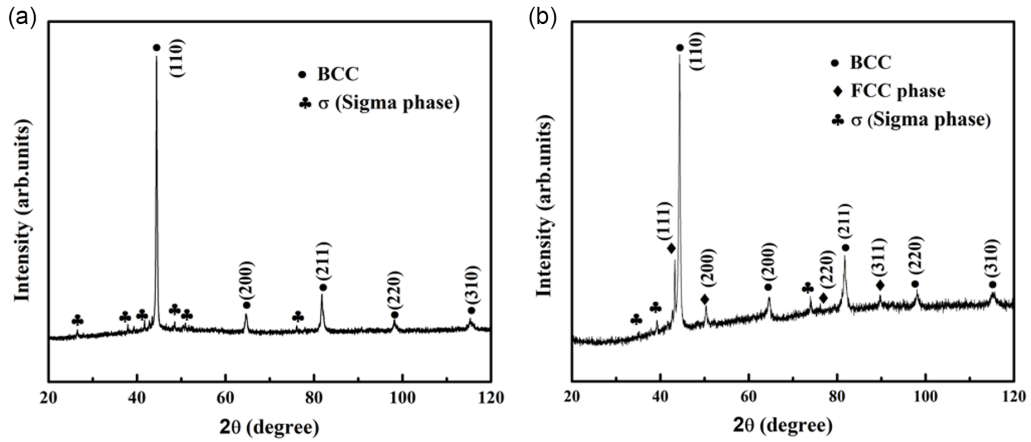

Figure 5. The X-ray diffraction pattern of SPSed AlCrFeCoNiZn HEA sample heat-treated at a) 800 °C and b) 900 °C for 2 h, followed by water quenching. The formation of BCC, FCC, and σ-type phase could be discerned.

to a significant extent. With increased milling time, a single-phase BCC structure was observed after 20 h. The milling time was further increased to 30 h to see whether there is any further phase change in the alloy. However, no noticeable difference was observed except for an increase in the broadening of the peaks. The 30 h milled powder showed formation of a single-phase BCC structure and Figure 3b shows the full pattern Rietveld refinement. The refined lattice parameter of the 30 h milled powder of the BCC phase was calculated to be 2.885 Å. The nanocrystalline nature of milled powder was confirmed through TEM. Figure 3c shows that the bright-field image contains nanostructured grains. The formation of ring pattern (inset image) in selected-area-electron diffraction (SAED) pattern suggests the polycrystalline nature of the 30 h milled powder with single-phase BCC structure, corroborating the XRD findings. The dark-field TEM image (Figure 3d) was captured using a (110) ring, showing the diffracted nanocrystals. The representative image shows the presence of crystals of different sizes (≈25–40 nm) that leads to the variations in intensity observed in the (110) ring of SAED pattern.

Figure 4a shows the diffraction pattern of SPS-prepared AlCrFeCoNiZn at 800 °C. Single-phase BCC structure of the alloy was observed even after sintering. The Rietveld refined pattern of the SPSed sample is given in Figure 4b and the refined value of the lattice parameter turns out to be 2.883 Å. While we see phase separation in EDS data for SPS-prepared alloy, the peaks for these phases appear to have been masked by the background in the XRD pattern owing to their low volume fractions. The absolute density of the sintered alloy, measured by Archimedes principle, is 6.40 g cc^{-1} against the rule of mixture density of 7.11 g cc^{-1}. The sintered pellets appeared dense and no visible porosity was observed in the SEM images. The DSC thermogram of the SPSed sample heated up to 1300 °C (Figure 4c) shows no sharp reaction up to 1000 °C. A small change in heat transient in the temperature range of 80–120 °C is possibly related to the release of the residual strain in the sample accumulated during milling. The broad temperature range (200–1000 °C) of thermal events in the DSC thermogram indicates that the formation of the different phases (presumably (Al, Cr)-rich and (Fe, Co)-rich phases) is diffusion controlled and occurs gradually. The same was confirmed via subsequent heat treatments at different temperatures and cooling conditions.

The SPS-prepared alloy was further subjected to three different heat-treatment schedules: 1) 800 °C for 2 h followed by water quenching; 2) 900 °C for 2 h followed by water quenching; and 3) 900 °C for 12 h followed by furnace cooling. The diffraction pattern of the sample heat-treated at 800 °C for 2 h followed by water quenching (**Figure 5**a) shows that new phases have formed along with the BCC phase. Careful indexing of the diffraction pattern confirms the formation of BCC phase along with the σ-type phase. The sample heat-treated at 900 °C shows the BCC and σ-type phases along with the evolution of FCC phase (Figure 5b).

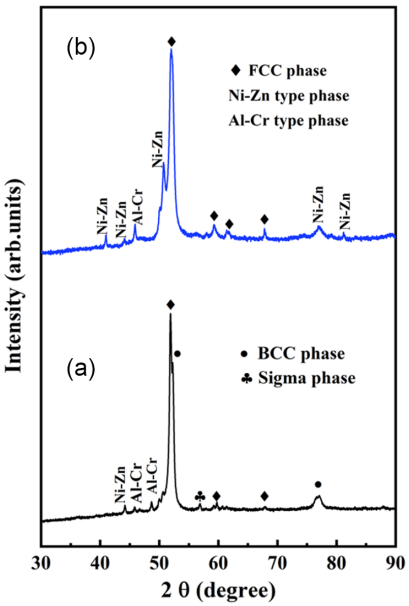

Figure 7. The X-ray diffraction plots of samples heat-treated at a) 900 °C and b) 1100 °C for 2 h, followed by furnace cooling. The Co-target was used to get the better diffraction intensity of evolved phases.

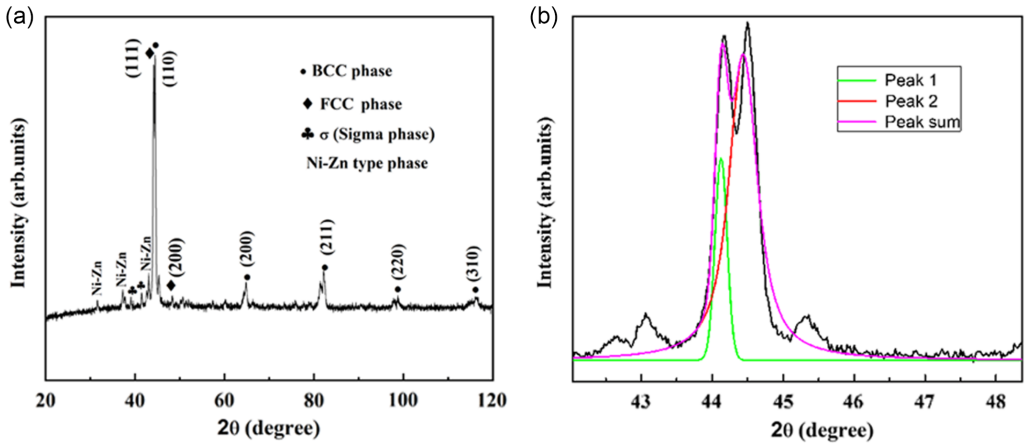

Figure 6. a) X-ray diffraction pattern of the SPS-prepared AlCrFeCoNi heat-treated at 900 °C for 12 h followed by furnace cooling. The formation of B2, FCC, and σ-type phase could be discerned along with the stable BCC phase. b) Deconvolution of the major peak.

To understand the stability of these evolved phases, another sample was heat-treated at 900 °C for 12 h followed by furnace cooling to drive the system toward equilibrium. The XRD pattern (**Figure 6**) shows the formation of Ni–Al-type B2 ($a = 2.86 \pm 0.01$ Å), FCC ($a = 3.59 \pm 0.02$ Å), and σ-type phase. We also looked at the diffraction plots of heat-treated samples at 900 and 1100 °C for 2 h in Co-target to get the better intensity plots (**Figure 7)** of evolved phase. The sample of 900 °C heat-treated conditions (Figure 7a) has shown the evolution of BCC (Co–Fe type, PDF#-00-049-1567), FCC, σ (Fe–Cr type, PDF#- 0071-7530), and Al–Cr type, PDF#-01-082-2599) phases. With increase in heat-treatment temperature of 1100 °C, the sample shows the more equilibrium phase of FCC, Ni–Zn (PDF#-01 = 085-7584, $a = 8.93$ Å, cI-52), and Al–Cr-type phase. These results are in agreement with the elemental segregation maps, predicted through ML.

2.3. Elemental Segregation and Phase Separation from EDS Data

The elemental maps (atomic percent) obtained from EDS were used to analyze the elemental segregation and phase separation

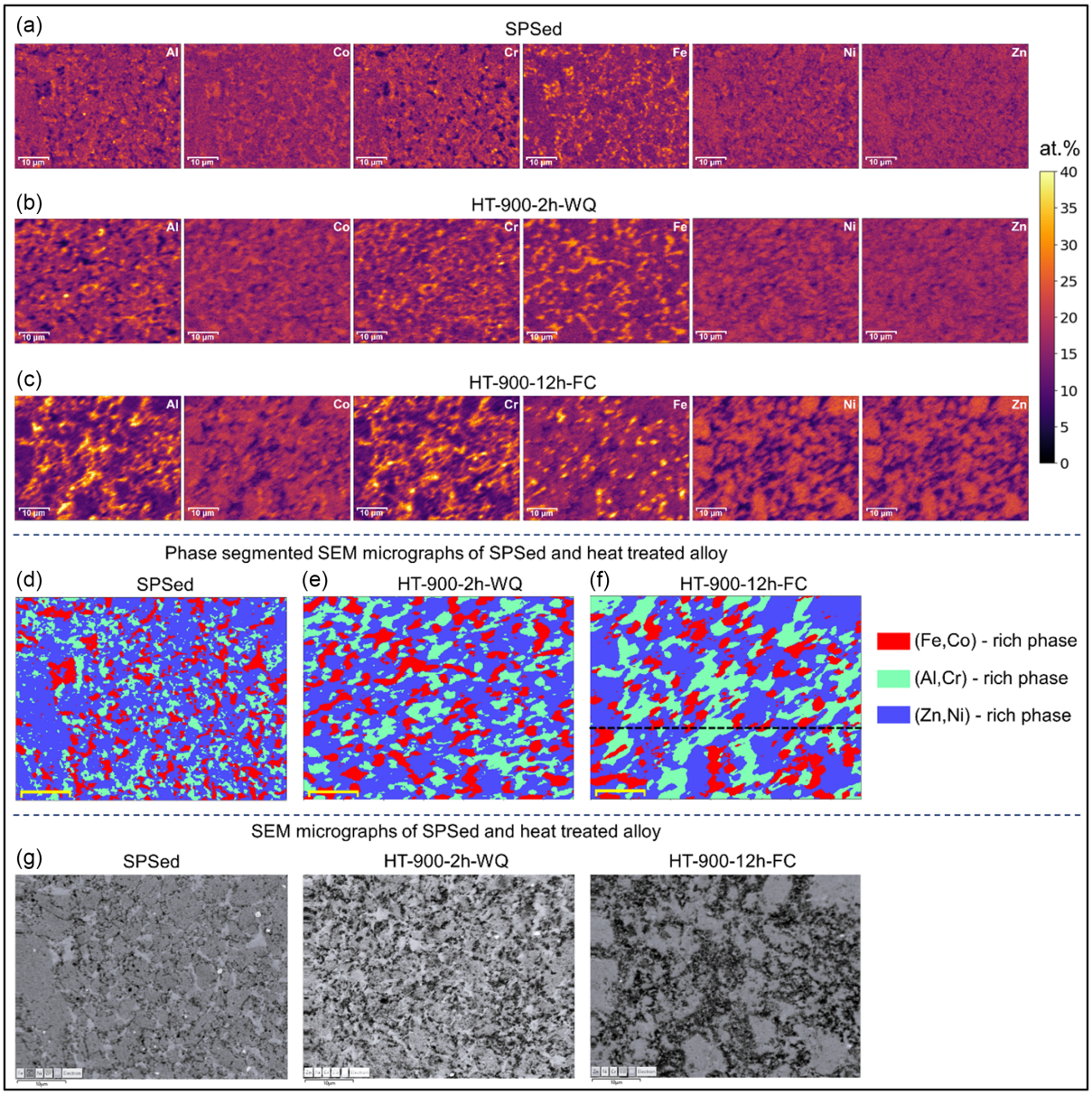

Figure 8. Elemental segregation and phase separation from energy-dispersive spectroscopy data. Element maps (atomic percent) for a) SPSed, b) heat-treated (HT) 900-2 h-water quenched (WQ), and c) HT-900-12 h-furnace cooled (FC) samples. Phase segmented microstructures of d) SPSed, e) HT-900-2 h-WQ, and f) HT-900-12 h-FC samples. g) SEM micrographs of SPSed and heat-treated samples. Here, "HT-900-2 h-WQ" represents sample HT at 900 °C for 2 h and WQ, "HT-900-12 h-FC" represents sample heat-treated at 900 °C for 12 h and FC. The black-dashed line in f) indicates the scan line profile for Figure 8. The scale bar used throughout this figure corresponds to 10 µm length.

behavior of AlCrFeCoNiZn following SPS and heat treatments, as seen in **Figure 8**. In SPSed sample (Figure 8a,d), the formation of a (Fe, Co)-rich phase, with very low Al and Cr content, is clearly evident. Al and Cr also appear to segregate together to form an (Al, Cr)-rich phase. Ni and Zn don't show any significant segregation in SPSed sample, although a slightly higher and lower Ni content is associated with (Al, Cr)-rich and (Fe, Co)-rich phases, respectively. Thus, the EDS maps for SPSed sample show signs of elemental segregation that was also predicted by the ML and the CALPHAD approach. But there are two key deviations. First, formation of an (Al, Cr)-rich phase is seen here which was neither predicted by the CALPHAD approach here nor has been reported in any previous studies on AlCrFeCoNi or related alloys. Second, the Zn segregation in SPSed sample is quite insignificant as compared to the expectations set by ML and CALPHAD approach. This prompted us to perform heat-treatment studies since SPS exposes the sample to high temperature for a very brief duration that may not be sufficient to form equilibrium structures.

Heat treatment at 900 °C for 2 h, followed by water quenching, shows similar segregation tendencies as SPSed sample with the formation of (Al, Cr)-rich and (Fe, Co)-rich phases, as seen in Figure 8b; although the size of these phases has increased after heat treatment, as seen in Figure 8e. Also, we see that Zn and Ni have started segregating together to form (Zn, Ni)-rich regions, although the extent of Zn segregation is still not too significant. Prolonged heat treatment at 900 °C for 12 h, followed by furnace cooling, makes the elemental segregation significantly pronounced even though the nature of segregation remains the same, as seen in Figure 8c. The size and volume of (Al, Cr)-rich phase increases considerably, as seen in Figure 8f, along with its Al and Cr content, resulting in large regions that are depleted in Al and Cr. In contrast, there is no significant change in the (Fe, Co)-rich phase. With prolonged heat treatment, Zn and Ni have segregated together to form a phase that contains appreciable Co and Fe but very low Al and Cr, as seen in Figure 8c. At the same time, (Al, Cr)-rich and (Fe, Co)-rich phases have been considerably depleted of Ni and Zn.

In brief, the heat treatment leads to elemental segregation resulting in the separation of system into three primary phases: (Zn, Ni)-rich, (Al, Cr)-rich, and (Fe, Co)-rich phase. The phase-segmented microstructures of SPSed and heat-treated alloys have been shown in Figure 8d–f. Since (Al, Cr)-rich phase has not been reported in any other studies on (AlCoCrFeNi)-based alloys, its formation here could be attributed to the presence of Zn which has a strong clustering tendency with respect to Cr.

Further analysis of the EDS data indicates that when the sample undergoes heat treatment at 900 °C for 12 h followed by furnace cooling, the (Al, Cr)-rich phase might be undergoing a separation into Cr-rich and Al-rich regions, as seen in **Figure 9**. The line scan indicates that this separation might be occurring over ≈1 µm distances (Figure 9c), but the spatial resolution of EDS maps here is not sufficient to make conclusive claims about the exact nature of this behavior. Future studies into this behavior may lead to more insights.

2.4. Electronic Structure of Equiatomic AlCrFeCoNiZn

To understand the ML and CALPHAD predictions and the experimental results, we performed a detailed electronic structure and thermodynamic analysis of the equiatomic AlCrFeCoNiZn alloy. The partial density of states (PDOS) of AlCrFeCoNiZn was compared in BCC and FCC phases. Singh et al.[12] have discussed the rules of solid-solution formation, where the energy of formation (E_{form}) range is $-11 \lesssim E_{form} \lesssim 5$ mRy (per atom). The E_{form} for BCC AlCrFeCoNiZn is $+5.48$ mRy atom^{-1} close to solid-solution formation range, while VEC (8.0) is much higher for BCC formation ($4 < VEC < 6.7$). In contrast, E_{form} of $+7.71$ mRy atom^{-1} in the FCC phase is higher for solid-solution phase formation; however, VEC (8.0) is just on the edge of FCC formation ($VEC > 8.0$). Recently, for multi-principal element alloys (MPEAs),[40] the *d* band filling and hybridization were shown to play significant role

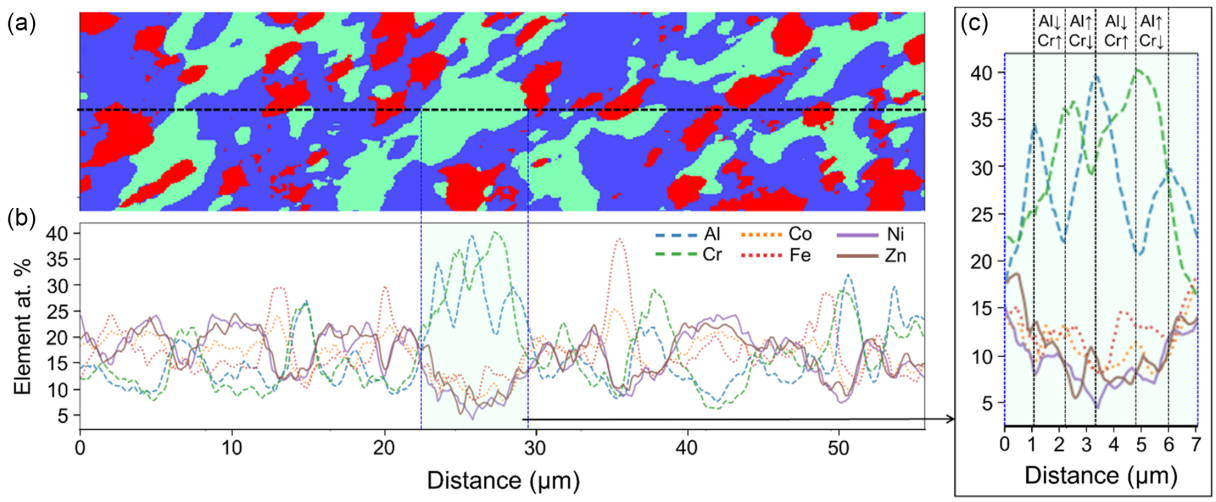

Figure 9. Line scan to probe phase separation within (Al, Cr)-rich phase in annealed sample (900 °C—12 h furnace cooled). a) Scan line profile in the segmented microstructure. b) Elemental distribution (atomic percent) plot along the scan line. c) Magnified view of region highlighted in (b). The scan line profile is also shown in Figure 7f.

in driving single-phase (BCC or FCC) stability. The higher positive E_{form} of FCC AlCrFeCoNiZn possibly restricts formation of single-phase alloy by reducing the number of unlike bonding pairs required for improved phase stability. The competing E_{form} and VEC in FCC and BCC phase can lead to energy instability of single-phase AlCrFeCoNiZn. However, the underlying thermodynamic and electronic reasons for this behavior are not obvious.

To understand the electronic origin, we plot (electronic) PDOS for of AlCrFeCoNiZn in **Figure 10**. The BCC phase in Figure 10a shows strong hybridized states near −0.08 Ry in the majority (up-spin) channel below the Fermi energy (E_{Fermi}) compared to FCC phase (Figure 10b). The reduced hybridization in BCC phase increases the filling of bonding states below E_{Fermi}; at the same time, it pushes antibonding (or nonbonding) states above E_{Fermi}. For the FCC phase (Figure 10b), we found strong disorder broadening that leads to weak hybridization and reduces the ordering strength. Both BCC (+5.48 mRy atom^{-1}) and FCC (+7.71 mRy atom^{-1}) phases show positive E_{form}, i.e., FCC is energetically higher by +2.23 mRy atom^{-1}. If we look closely at PDOS in minority (down-spin) channel, FCC phase in Figure 10b has disorder broadened Co-3*d* peak at EFermi, while the same peak is slightly away from E_{Fermi} in BCC phase. The Co-3*d* gains more charges in FCC versus BCC phase that pushes the Co-3*d* to E_{Fermi} and enhances the energy instability.

We also assessed the SRO in FCC AlCrFeCoNiZn to understand the change in probability distribution of each element on sublattices of $L1_2$ phase, compared to disordered phase. The SRO analysis suggests that Cr–Fe–Zn and Al–Ni–Co preferably go, respectively, to 1a (000) and 3c (0 ½ ½) positions in the $L1_2$ phase. This explains the phase stability in this system as E_{form} in $L1_2$ phase is −0.55 mRy atom^{-1}, lower than both BCC (+5.48 mRy atom^{-1}) and FCC (7.71 mRy atom^{-1}). Formation enthalpy alone does not explain the kinetically slow diffusion transformation to $L1_2$ phase from BCC precursors;[41] however, the low {111} stacking-fault energies in addition to the large free-energy barrier are known to enable such transformations.[42]

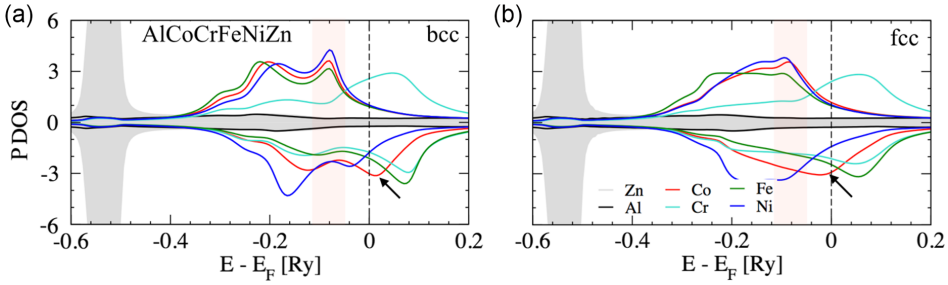

Figure 10. DFT partial density of states in a) BCC and b) FCC phases for AlCrFeCoNiZn HEA.

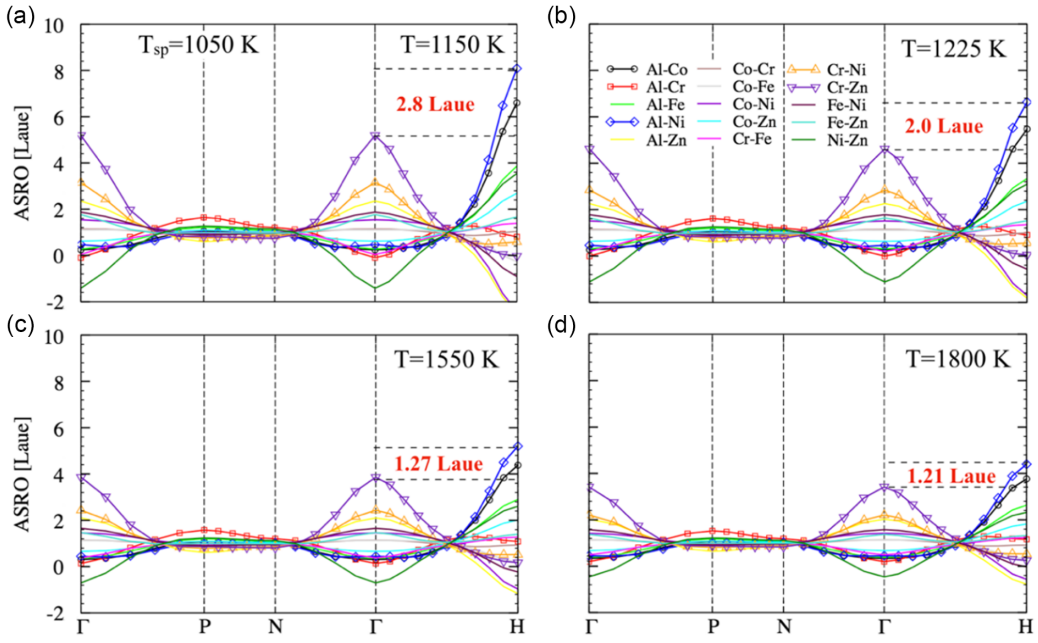

Figure 11. Warren–Cowley SRO parameters [$\alpha_{\mu\nu}$ (*k*;T)] in Laue units for AlCrFeCoNiZn plotted above the spinodal temperature ($T_{sp} \approx 1050$ K) at a) 1150 K, b) 1225 K, c) 1550 K, and d) 1800 K. The SRO is plotted along BCC high-symmetry Brillouin zone directions.

The stacking-fault energy (SFE) in the FCC phase of AlCrFeCoNiZn is 5.4 mJ m^{-2}; interestingly, a low SFE supports the kinetically slow diffusion transformation formation of $L1_2$ phase.

In contrast, a positive formation enthalpy (+5.48 mRy $atom^{-1}$) for BCC AlCrFeCoNiZn suggests weak thermodynamic stability, while strong hybridization in Figure 10a shows tendency of ordering interaction in BCC phase. Moreover, experiments in Figure 8 found (Zn, Ni)-rich, (Al, Cr)-rich, and (Fe, Co)-rich phases that suggests that certain elements lead to increased chemical interactions in BCC phase. We also found this behavior through increased hybridization in PDOS analysis in Figure 10a. To understand this better, we plot temperature dependence of Warren–Cowley parameters in **Figure 11**, which is a thermodynamic representation of increased interactions due to infinitesimal change in local chemical concentration fluctuations, i.e., SRO.[12,40,43–45]

The SRO in Figure 11 shows peak at H [111] point, with Al–Ni as dominant pair in AlCrFeCoNiZn. Interestingly, the Al–Ni pair with peak at H point in Figure 11b is the most dominant SRO mode that shows the ordering (B2-type) interaction. The dominant SRO pairs reveals the unstable (Fourier) modes with ordering wavevector (k_o) or phase separation (clustering at k_o = (000)) at spinodal temperature ($T_{sp} \approx 1050$ K).[12,40,43–45] Despite decreasing SRO strength of Al–Ni pair from 2.80 Laue at 1150 K to 1.21 Laue at 1800 K, the Al–Ni pair remains dominant at all temperatures. Interestingly, we also found stronger and competing clustering pairs (Cr–Zn and Cr–Ni) with peak at Γ (=000) at higher temperatures, suggesting that energetically Cr does not prefer to sit in the neighborhood of Zn/Ni. Therefore, if the opportunity arises, Cr will phase separate with both Ni and Zn. This is further affirmed through clustering tendency of Cr–Ni/Cr–Zn pairs (with peak at the Γ point) and ordering tendency of Ni–Zn (with peak at the *H* point), as shown in Figure 11. This finding is in agreement with our experiments in Figure 8d–f that shows formation of (Zn, Ni)-rich phases. Moreover, the peak in DSC measurements at 1063 K, where some of the decompositions occur, is very close to our predicted spinodal temperature (1050 K).

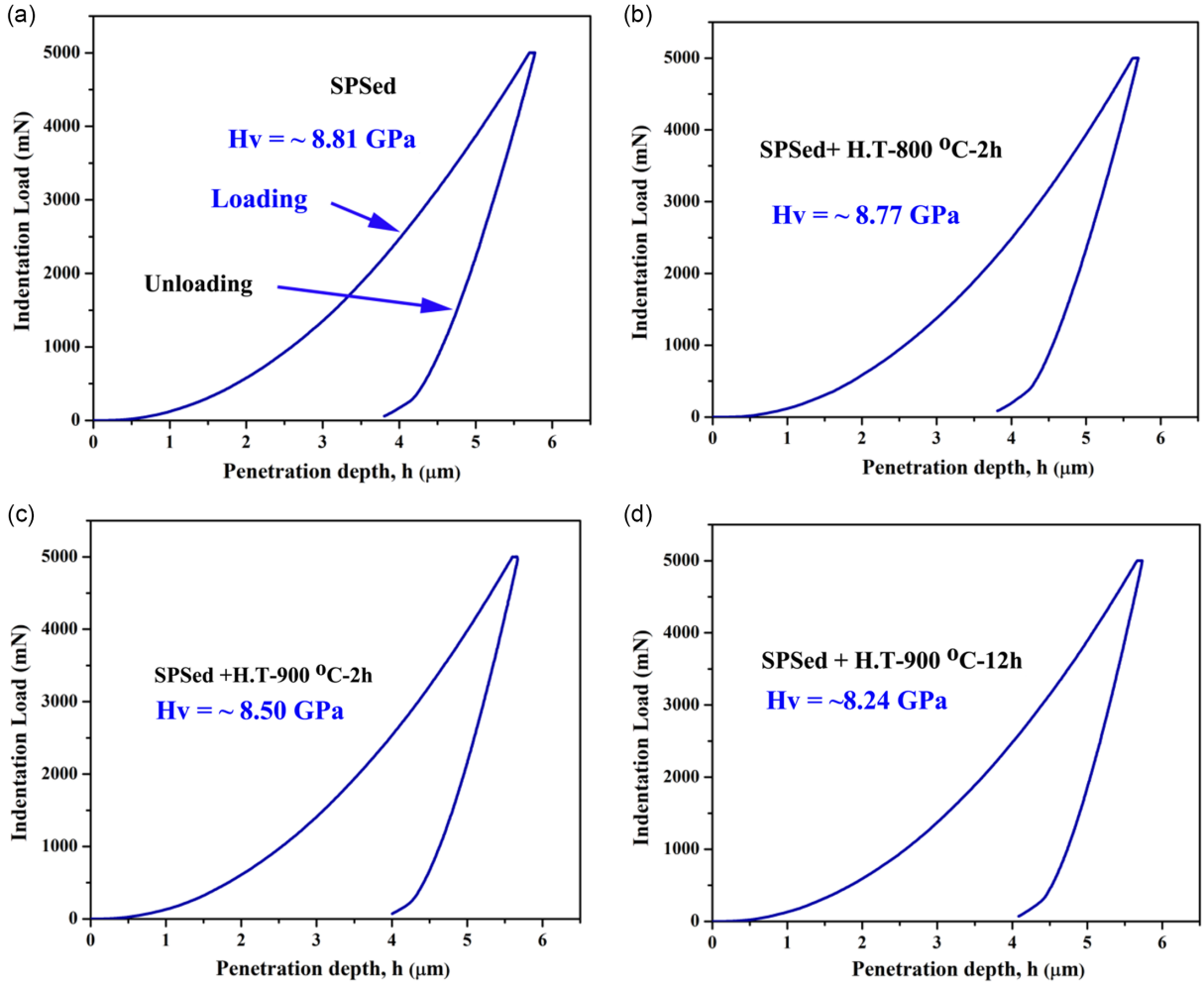

Figure 12. Load (mN) versus penetration depth (μm) plots of AlCrFeCoNiZn for the following: a) as SPS prepared, b) heat-treated at 800 °C followed by water quenching, c) heat-treated at 900 °C for 2 h followed by water quenching, and d) heat-treated at 900 °C for 12 h followed by furnace cooling. Corresponding values of hardness (Hv) is given in the respective plots.

Table 1. Microhardness, elastic modulus, and estimated yield strength of consolidated AlCrFeCoNiZn HEA at different conditions.

Sample condition	Microhardness (H_v) [GPa] load—5000 mN	Elastic modulus (E) [GPa]	Estimated yield strength (σ_y) [GPa]
SPS-prepared	8.81	149	2.93
SPSed+ annealed at 800 °C for 2 h—water quenched	8.77	163	2.92
SPSed+ annealed at 900 °C for 2 h—water quenched	8.50	182	2.83
SPSed+ annealed at 900 °C for 12 h—furnace cooled	8.24	185	2.74

2.5. Mechanical Response of AlCrFeCoNiZn

The mechanical response of SPS-prepared and heat-treated samples was studied using the Vickers microhardness-instrumented indentation technique. The plots of the applied load and depth of penetration have been shown in **Figure 12**. The hardness and elastic modulus (E) for the SPS-prepared sample was measured as ≈8.81 and 149 GPa, respectively. Upon heat treatment at 800 and 900 °C for 2 h, the hardness decreased to ≈8.77 and 8.50 GPa, respectively, whereas the elastic modulus increased to 163 and 182 GPa, respectively, reflecting the changes in phase compositions. The sample heat-treated at 900 °C for 12 h followed by furnace cooling yielded a hardness of ≈8.24 GPa with an elastic modulus of ≈185 GPa. The alloy's yield strength was estimated using Tabor's equation, $\sigma_y = H_v/3$; where σ_y is yield-strength (GPa) and H_v is the hardness (GPa). The results of hardness (Hv), elastic modulus (E), and yield strength (σ_y) are summarized in **Table 1**. No indentation cracks were observed in the micrographs, as seen in Figure S3, Supporting Information. The higher hardness values in the SPSed and heat-treated samples are the resultant of the nanostructured grains formation and precipitation of IM compounds of (Al, Cr)-rich, (Fe, Co)-rich, and (Zn, Ni)-rich phases, respectively.

3. Conclusions

While Al addition is known to cause transition from FCC to BCC in $Al_x(CoCrFeNi)_{1-x}$ (owing to considerable reduction in VEC), the addition of Zn to AlCrFeCoNi poses exciting and open questions as to how it would affect the phase evolution. The Zn has a high VEC that should stabilize FCC phase, while it exhibits ordering tendency with Ni and Co and strong clustering tendency with Cr and Fe, thereby hinting toward phase separation. To address these questions, we probed the phase evolution in AlCrFeCoNiZn using a combination of experimental (XRD, SEM, EDS, and DSC) and computational (ML, CALPHAD, and DFT) techniques. It is important to understand that phase evolution in high-entropy chemically complex system is a problem that is still being probed scientifically and that a combination of techniques rather than a single modeling approach is required to gain a deeper understanding of the system.

To conclude, we find the following: 1) A strong clustering tendency of Cr–Zn and Cr–Ni pairs, combined with the strong ordering of Zn–Ni pair, drives out the Cr that in turn combines with Al to form an (Al, Cr)-rich phase. This study reports formation of (Al, Cr)-rich phases in (AlCrFeCoNi)-based HEAs that usually end up with (Al, Ni)-rich phases or IMs due to the strong ordering tendency of Al–Ni pair that is disturbed due to the presence of Zn; 2) The AI/ML model accurately predicts the tendency of IM phase formation; however, the lack of training data for IM type prevents from identifying the ordering phases. In contrast, we attribute the erroneous CALPHAD predictions to the lack of a well-assessed database for Zn–HEAs; 3) The mechanically alloyed AlCrFeCoNiZn HEA powder shows single-phase BCC structure. However, sintering and subsequent heat treatments lead to phase separation resulting in formation of (Al, Cr)-rich, (Fe, Co)-rich, and (Zn, Ni)-rich phases; 4) Phase separation observed in AlCrFeCoNiZn upon heat treatment is diffusion controlled and occurs because of gradual elemental segregation as no sharp phase-transition peaks were observed in the DSC from room temperature to 1000 °C; and 5) The thermodynamic stability of $L1_2$ phase arises from a considerably lower formation energy when Cr–Fe–Zn and Al–Ni–Co preferably goes to 1a (000) and 3c (0 ½ ½) positions, respectively. The kinetically slow-diffusion transformation to $L1_2$ phase from BCC precursors is made possible by the small SFE of AlCrFeCoNiZn.

The slow diffusion-controlled transformation leading to formation of (Al, Cr)-rich phase may possibly be linked to the solute-drag effect induced by the addition of Zn, similar to how the addition of Sn slows the growth kinetics in FeCoNiCuSn alloy.[46] A similar effect has also been seen in Al–CrFeNi alloys wherein relatively small changes in Al solute concentration result in different diffusion and growth behavior.[47] Future studies are required to ascertain the exact nature of this behavior.

4. Experimental Section

Experimental Methods: High-purity (>99%) elemental powders of Al, Co, Cr, Fe, Ni, and Zn with average particle sizes of 45 μm were used as the starting material. The initial mixture of the elemental powder was taken in equiatomic proportion, mixed at room temperature, and subjected to the initial structural confirmation through XRD. The mixed elemental powder was apportioned into two vials of 250 mL capacity, with 30 g powder in each. Milling was carried out in a high-energy planetary ball mill (Retsch PM 400) using tungsten-carbide vials and balls of 10 mm diameter with the rotation speed of 200 rpm. The wet medium of milling was adopted by using toluene as a processing control agent with a ball to powder ratio of 10:1. A definite protocol of milling was utilized, in which the mill was stopped for half an hour after every hour of milling to avoid the overheating of the vial temperature. The powder was collected at every 10 h of milling to do the phase evolution study. Milling was done for a total of 30 h duration to avoid the contamination of milled powder. The 30 h milled powder was further subjected to consolidation through SPS at 800 °C with a holding time of 15 min under 50 MPa pressure. The SPS-prepared sample was further sectioned into three small pieces (diametrically) and sealed into the vacuum quartz tube for heat treatments. These quartz tubes were backfilled with argon gas to avoid

the oxidation of samples. Two samples were heat-treated at 800 and 900 °C for 2 h, followed by water quenching. In another case, a sample was heat-treated at 900 °C for the holding time of 12 h, followed by furnace cooling to understand (by comparing with quenched samples) the extent to which kinetics affect the phase evolution.

XRD (Rigaku MiniFlex: 600 W; Cu Kα radiation, $\lambda = 1.541$ Å) with a Bragg–Brentano geometry, operated at 20 kV and 40 mA with a scanning speed = 10° min^{-1}, was used to study the structural changes in the milled, SPSed, and heat-treated samples. Additional XRD studies were also carried out using a Co Kα radiation, $\lambda = 1.789$ Å radiation to minimize fluorescence. The evolved phases were analyzed using the International Centre for Diffraction Data (ICDD) base software. The XRD data was processed through Rietveld refinement using the Generalized Structure Analysis System(GSAS-2)[48] to quantify the changes in the lattice parameter in milled and SPSed samples. The nanostructured nature of the 30 h milled powder was confirmed through TEM (Model FEI TECNAI G^2 T20) operated at 200 kV. The sample preparation for TEM involves dispersion of small amount of powder in acetone/ethanol followed by 10–20 min of ultrasonication to produce agglomeration-free suspension. After sonicating the solution, a single drop was placed on a copper grid. For microstructural characterization, the samples were mechanically polished by following the standard metallographic steps and were subsequently etched in the dilute aqua regia solution (hydrochloric acid and nitric acid in a 3:1 molar ratio). The microstructures were examined using a scanning electron microscope (SEM, Model: FEI, Quanta 200F and ZEISS, EVO) operated at 30 and 20 kV and equipped with EDS detector. The absolute density of the SPSed sample was measured by following the Archimedes principle using distilled water as a medium. Thermal stability of SPS-prepared alloy was studied by differential scanning calorimetry (DSC-404-F3 Pegasus, Netzsch) with suitable heat treatments. The mechanical response of the samples in the SPSed and heat-treated conditions were evaluated through microhardness instrumented indentation tester (MHT^3, Anton Paar) at a load of 500 mN with the loading and unloading rate of 1000 mN min^{-1}. The indents were observed through the optical microscope retrofitted with the instrument are given in Figure S3, Supporting Information. Minimum of 10 measurements were done to calculate the average microhardness value. The hardness of the samples were computed through Oliver–Pharr method.[49]

ML and CALPHAD Predictions: For ML predictions, a pretrained model[36] was used to calculate the phase fractions of FCC, BCC, and intermetallic (IM) phases. This model comprised a neural-network ensemble that took 14 alloy features as input to predict phase fractions, and it was shown to predict phase fractions accurately in a variety of HEAs.[36] CALPHAD calculations were performed using Thermo-Calc with TCHEA5 database that has been developed for HEAs.

DFT and SRO: The DFT-based Korringa–Kohn–Rostoker (KKR) method (a Greens' function theory) combined with the coherent potential approximation (CPA) was used to calculate total energy of arbitrary solid-solution alloys.[50] The KKR–CPA performs configurational averaging over all configurations in infinite lattice simultaneously with DFT charge self-consistency, and properly includes alloy-induced Friedel impurity-charge screening. For DFT, we used the Perdew–Burke–Ernzerhof exchange–correlation functional for solids.[51] An equally spaced k-space mesh of $24 \times 24 \times 24$ was used for Brillouin-zone integrations. The core electrons were treated fully relativistically (includes spin–orbit coupling), while semi-core/valence electrons were treated scalar relativistically (i.e., neglecting spin–orbit coupling). Warren–Cowley SRO parameters $\alpha^{ij}_{\mu\nu}$ (μ, ν denote elemental occupations of sites i,j in a Bravais lattice) were calculated from thermodynamic linear-response theory[12,40,43–45] using homogeneous alloy composition $\{c^i_\mu\}$ as a reference. For a homogeneous solid-solution alloy with $\{c^i_\mu\}$, the SRO dictated pair probabilities $P^{ij}_{\mu\nu} c^i_\mu c^j_\nu (1 - \alpha^{ij}_{\mu\nu})$ that could affect chemical SRO, as well as mechanical behaviour.[52] For a dominant k-space wavevector, $k = k_o$, the SRO diverged at the spinodal temperature (T_{sp}) due to absolute instability to the correlated fluctuations, which provided an estimate for SRO and the order–disorder or miscibility temperature.[12] This first-principles theory of SRO was based on the electronic structure of the alloy; therefore, it directly embodied underlying electronic and alloying effects (like band-filling, hybridization, or Fermi-surface nesting.[53]

Supporting Information

Supporting Information is available from the Wiley Online Library or from the author.

Acknowledgements

Authors would like to thank the editors for the invitation to contribute in this special issue of Advanced Engineering Materials in honour of Professor C. Suryanarayana in order to recognition of his outstanding contribution in Materials Research. V.S. and N.K.M. would like to acknowledge Prof. R.K.M., Dr. R.M., Dr. V.C.S., and Dr. J.B. for their useful discussion and help during the experimental investigations. V.S. also acknowledges the support from IIT Ropar in the form of an institute postdoctoral fellowship. P.K.R. acknowledges the support from IIT Ropar's ISIRD-II program. The theoretical work (including DFT-based methods in HEAs) at Ames Laboratory (Ames Laboratory is operated by Iowa State University for the US DOE under contract DE-AC02-07CH11358) was supported by U.S. Department of Energy (DOE), Office of Science, Basic Energy Sciences, Materials Science & Engineering Division.

Conflict of Interest

The authors declare no conflict of interest.

Author Contributions

Vikas Shivam: Conceptualization (lead); Formal analysis (lead); Investigation (lead); Methodology (equal); Writing—original draft (lead). **Dishant Beniwal**: Formal analysis (supporting); Investigation (equal); Methodology (equal); Writing—review & editing (equal). **Yagnesh Shadangi**: Investigation (supporting); Writing—review & editing (supporting). **Prashant Singh**: Investigation (supporting); Writing—review & editing (equal). **Olena Palasyuk**: Investigation (supporting). **V. S. Hariharan**: Investigation (supporting). **M. J. Kramer**: Supervision (supporting); Writing—review & editing (supporting). **Gandham Phanikumar**: Investigation (supporting); Writing—review & editing (supporting). **Duane D. Johnson**: Investigation (supporting); Writing—review & editing (supporting). **Pratik K. Ray**: Investigation (lead); Project administration (lead); Supervision (lead); Writing—review & editing (lead). **Nilay Krishna Mukhopadhyay**: Conceptualization (supporting); Investigation (supporting); Supervision (lead); Writing—review & editing (lead). All authors participated in writing the manuscript.

Data Availability Statement

The data that support the findings of this study are available from the corresponding author upon reasonable request.

Keywords

density-function theories, high-entropy alloys, machine learning, mechanical alloyings, phase evolutions

Received: April 5, 2024
Revised: September 2, 2024
Published online: September 24, 2024

[1] J.-W. Yeh, S.-K. Chen, S.-J. Lin, J.-Y. Gan, T.-S. Chin, T.-T. Shun, C.-H. Tsau, S.-Y. Chang, *Adv. Eng. Mater.* **2004**, *6*, 299.
[2] B. Cantor, I. T. H. Chang, P. Knight, A. J. B. Vincent, *Mater. Sci. Eng., A* **2004**, *375–377*, 213.
[3] E. P. George, W. A. Curtin, C. C. Tasan, *Acta Mater.* **2020**, *188*, 435.
[4] E. P. George, D. Raabe, R. O. Ritchie, *Nat. Rev. Mater.* **2019**, *4*, 515.
[5] D. B. Miracle, O. N. Senkov, *Acta Mater.* **2017**, *122*, 448.
[6] B. S. Murty, J. W. Yeh, S. Ranganathan, P. P. Bhattacharjee, in *High-Entropy Alloys*, 2nd ed., Elsevier, **2019**, https://doi.org/10.1016/C2017-0-03317-7.
[7] Z. Li, K. G. Pradeep, Y. Deng, D. Raabe, C. C. Tasan, *Nature* **2016**, *534*, 227.
[8] E. Ma, X. Wu, *Nat. Commun.* **2019**, *10*, 5623.
[9] S. Wei, F. He, C. C. Tasan, *J. Mater. Res.* **2018**, *33*, 2924.
[10] H. Huang, Y. Wu, J. He, H. Wang, X. Liu, K. An, W. Wu, Z. Lu, *Adv. Mater.* **2017**, *29*, 1701678.
[11] Y. F. Ye, Q. Wang, J. Lu, C. T. Liu, Y. Yang, *Mater. Today* **2016**, *19*, 349.
[12] P. Singh, A. Sharma, A. V. Smirnov, M. S. Diallo, P. K. Ray, G. Balasubramanian, D. D. Johnson, *npj Comput. Mater.* **2018**, *4*, 16.
[13] F. He, Z. Wang, Q. Wu, J. Li, J. Wang, C. T. Liu, *Scr. Mater.* **2017**, *126*, 15.
[14] S. Yang, J. Lu, F. Xing, L. Zhang, Y. Zhong, *Acta Mater.* **2020**, *192*, 11.
[15] S. Guo, C. Ng, J. Lu, C. T. Liu, *J. Appl. Phys.* **2011**, *109*, 103505.
[16] R. Chen, G. Qin, H. Zheng, L. Wang, Y. Su, Y. Chiu, H. Ding, J. Guo, H. Fu, *Acta Mater.* **2018**, *144*, 129.
[17] V. Shivam, V. Sanjana, N. K. Mukhopadhyay, *Trans. Indian Inst. Met.* **2020**, *73*, 821.
[18] V. Shivam, J. Basu, Y. Shadangi, M. K. Singh, N. K. Mukhopadhyay, *J. Alloys Compd.* **2018**, *757*, 87.
[19] V. Shivam, S. Kar, G. K. Bansal, A. K. Chandan, B. K. Sahoo, G. K. Mandal, N. K. Mukhopadhyay, V. C. Srivastava, *J. Alloys Compd.* **2023**, *952*, 170029.
[20] V. Shivam, J. Basu, R. Manna, N. K. Mukhopadhyay, *Metall. Mater. Trans., A* **2021**, *52*, 1777.
[21] H. P. Chou, Y. S. Chang, S. K. Chen, J. W. Yeh, *Mater. Sci. Eng., B* **2009**, *163*, 184.
[22] W. R. Wang, W. L. Wang, S. C. Wang, Y. C. Tsai, C. H. Lai, J. W. Yeh, *Intermetallics* **2012**, *26*, 44.
[23] T. Roy, V. Shivam, K. Chattopadhyay, R. Manna, N. K. Mukhopadhyay, *Trans. Indian Inst. Met.* **2021**, *74*, 2093.
[24] S. Koul, V. Shivam, K. Chattopadhyay, R. Manna, K. Biswas, N. K. Mukhopadhyay, *J. Mater. Eng. Perform.* **2022**, *31*, 9522.
[25] Y. Shadangi, S. Sharma, V. Shivam, J. Basu, K. Chattopadhyay, B. Majumdar, N. K. Mukhopadhyay, *J. Alloys Compd.* **2020**, *828*, 154258.
[26] C. Suryanarayana, *Research* **2019**, *2019*, 228.
[27] M. Vaidya, G. M. Muralikrishna, B. S. Murty, *J. Mater. Res.* **2019**, *34*, 664.
[28] N. Singh, Y. Shadangi, V. Shivam, N. K. Mukhopadhyay, *J. Alloys Compd.* **2021**, *875*, 159923.
[29] H. Jain, Y. Shadangi, V. Shivam, D. Chakravarty, Dibyendu Mukhopadhya, N. K. Kumar, *J. Alloys Compd.* **2020**, *834*, 155013.
[30] V. Shivam, Y. Shadangi, J. Basu, N. K. Mukhopadhyay, *J. Mater. Res.* **2019**, *35*, 787.
[31] A. Munitz, S. Salhov, S. Hayun, N. Frage, *J. Alloys Compd.* **2016**, *683*, 221.
[32] V. Shivam, J. Basu, V. K. Pandey, Y. Shadangi, N. K. Mukhopadhyay, *Adv. Powder Technol.* **2018**, *29*, 2221.
[33] S. Mohanty, T. N. Maity, S. Mukhopadhyay, S. Sarkar, N. P. Gurao, S. Bhowmick, K. Biswas, *Mater. Sci. Eng., A* **2017**, *679*, 299.
[34] A. Manzoni, H. Daoud, R. Völkl, U. Glatzel, N. Wanderka, *Ultramicroscopy* **2013**, *132*, 212.
[35] P. Singh, D. D. Johnson, J. Tiarks, E. M. H. White, A. B. Kustas, J. W. Pegues, M. R. Jones, H. Lim, F. W. DelRio, J. D. Carroll, G. Ouyang, M. J. Abere, R. Naorem, H. Huang, T. M. Riedemann, P. G. Kotula, I. E. Anderson, N. Argibay, *Acta Mater.* **2024**, *272*, 119952.
[36] D. Beniwal, P. K. Ray, *Comput. Mater. Sci.* **2021**, *197*, 110647.
[37] D. Beniwal, P. Singh, S. Gupta, M. J. Kramer, D. D. Johnson, P. K. Ray, *npj Comput. Mater.* **2022**, *8*, 153.
[38] D. Beniwal, P. K. Ray, *Materialia*, **2022**, *26*, 101632.
[39] D. Beniwal, P. K. Jhalak, in *Forcefields for Atomistic-Scale Simulations: Materials and Applications* (Eds: A. Verma, S. M. Rangappa, S. Ogata, S. Siengchin), Springer, Singapore **2022**.
[40] P. Singh, A. V. Smirnov, D. D. Johnson, *Phys. Rev. B.* **2015**, *91*, 224204.
[41] M. Elzain, A. Gismelseed, A. Al-Rawas, A. Yousif, H. Widatallah, M. Al-Azri, M. Al-Barwani, *Hyperfine Interact.* **2016**, *237*, 8.
[42] J. Gou, T. Yang, X. Liu, T. Ma, *J. Alloys Compd.* **2020**, *836*, 155282.
[43] P. Singh, S. Picak, A. Sharma, Y. I. Chumlyakov, R. Arroyave, I. Karaman, D. D. Johnson, *Phys. Rev. Lett.* **2021**, *127*, 115704.
[44] P. Singh, S. Gupta, S. Thimmaiah, B. Thoeny, P. K. Ray, A. V. Smirnov, D. D. Johnson, M. J. Kramer, *Acta Mater.* **2020**, *194*, 540.
[45] P. Singh, A. V. Smirnov, A. Alam, D. D. Johnson, *Acta Mater.* **2020**, *189*, 248.
[46] M. R. Rahul, G. Phanikumar, *Mater. Sci. Eng., A* **2020**, *777*, 139022.
[47] X. J. Zuo, Y. Coutinho, S. Chatterjee, N. Moelans, *Mater. Theory* **2022**, *6*, 12.
[48] B. H. Toby, R. B. Von Dreele, *J. Appl. Crystallogr.* **2013**, *46*, 544.
[49] W. C. Oliver, G. M. Pharr, *J. Mater. Res.* **1992**, *7*, 1564.
[50] D. D. Johnson, D. M. Nicholson, F. J. Pinski, B. L. Gyorffy, G. M. Stocks, *Phys. Rev. Lett.* **1986**, *56*, 2088.
[51] J. P. Perdew, K. Burke, M. Ernzerhof, *Phys. Rev. Lett.* **1996**, *77*, 3865.
[52] J. Ding, Q. Yu, M. Asta, R. O. Ritchie, *Proc. Natl. Acad. Sci.* **2018**, *115*, 8919.
[53] P. Singh, A. V. Smirnov, D. D. Johnson, *Phys. Rev. Mater.* **2018**, *2*, 055004.